



ELSEVIER

Journal of Power Sources 163 (2007) 793–806

POWER
SOURCES

www.elsevier.com/locate/jpowsour

Transient non-isothermal model of a polymer electrolyte fuel cell

A.A. Shah^{a,*}, G.-S. Kim^b, P.C. Sui^c, D. Harvey^b^a Queen's-RMC Fuel Cell Research Centre, 945 Princess Street, Kingston, Ont. K7L 5L9, Canada^b Ballard Power Systems, 4343 North Fraser Way, Burnaby, BC V5J 5J9, Canada^c Institute for Integrated Energy Systems, University of Victoria, Victoria, BC V8W 3P6, Canada

Received 21 July 2006; received in revised form 8 August 2006; accepted 15 September 2006

Available online 7 November 2006

Abstract

In this paper we present a one-dimensional transient model for the membrane electrode assembly of a polymer-electrolyte fuel cell. In earlier work we established a framework to describe the water balance in a steady-state, non-isothermal cathode model that explicitly included an agglomerate catalyst layer component. This paper extends that work in several directions, explicitly incorporating components of the anode, including a micro-porous layer, and accounting for electronic potential variations, gas convection and time dependence. The inclusion of temperature effects, which are vital to the correct description of condensation and evaporation, is new to transient modelling. Several examples of the modelling results are given in the form of potentiostatic sweeps and compared to experimental results. Excellent qualitative agreement is demonstrated, particularly in regard to the phenomenon of hysteresis, a manifestation of the sensitive response of the system to the presence of water. Results pertaining to pore size, contact angle and the presence of a micro-porous layer are presented and future work is discussed.

© 2006 Published by Elsevier B.V.

Keywords: Fuel cell; Polymer-electrolyte; Transient model; Sweep simulations; Liquid water; Performance

1. Introduction

The proton exchange membrane fuel cell (PEMFC) is a promising source of clean and efficient energy, particularly for application in the automotive industry. As with other fuel cells, the basic principle of the PEMFC is to convert chemical into electrical energy. This aim is achieved by oxidation of hydrogen at the anode and simultaneous oxygen reduction at the cathode, with a net production of water. The reactants are delivered through a graphite paper, termed the gas diffusion layer (GDL), and reaction takes place in thin regions termed the catalyst layers. The catalyst in question is platinum (Pt), which is required to enhance the rate of reaction by providing an alternative pathway to the final products. Clearly, optimal use of the Pt is a key concern in all PEMFC designs.

The catalyst layers are perhaps the most complex components of the fuel cell. Through the solid components (carbon grains, supporting smaller catalyst particles, and electrolyte),

flow water vapour and components of air. Liquid water resides in the gas pores and absorbed water within the electrolyte. The electrons migrate through the carbon components of the layer while the protons migrate through pathways provided by the electrolyte—typically Nafion. The hydrophilic regions in the cathode catalyst layer (CCL) can cause retention of the water produced during reaction, which restricts the ingress of oxygen. Moreover, reaction is limited by the availability of Pt, and can only occur at points of contact between the Pt, carbon and electrolyte.

The properties of the membrane and the GDL, with possibly a micro-porous layer, also play a central role in the control of water. It is essential that the protons generated at the anode reach the cathode freely, requiring that the membrane remain well hydrated. The GDL must allow sufficient oxygen from the cathode channel to enter the CCL, but must be sufficiently hydrophobic to expel any build-up of liquid water beyond that required for optimal hydration of the membrane. The importance of water management explains the emphasis placed on capturing the effects of (particularly) liquid water in modelling studies [1–9]. However, a lack of understanding of the interaction between, and transport of, the three phases of water continues to retard progress towards a predictive model.

* Corresponding author. Tel.: +1 778 288 4292; fax: +1 604 268 6657.

E-mail address: ashah@pims.math.ca (A.A. Shah).

Steady-state PEMFC models are numerous. Because of the many challenges faced with the task of modelling the complex physics and geometry, a host of simplifying assumptions are regularly adopted, typically involving the catalyst layers, liquid water, electron transport, thermal energy and time dependence. For example, Natarajan and Nguyen [5], use a simplified and regularized form of the liquid water permeability in their isothermal model and do not explicitly model the membrane, catalyst layer and anode. Siegel et al. [6], incorporate the CCL and membrane, making the assumption that water exists only as vapour or as a species dissolved in the electrolyte/membrane, and are not able to account for liquid water effects directly. The same is true of the model in [10], which treats all three forms of water as a single phase. In [7], all three forms are included but with a highly regularized capillary diffusion coefficient. In [11–14], and references therein, the authors describe the water balance using the so-called multi-phase mixture (M^2) model, developed in [15], where thermodynamic equilibrium between liquid water and vapour is assumed to prevail throughout (saturated gas phase and no vapour diffusion) and saturation is calculated *a-posteriori* based on the equilibrium assumption and mixture water concentration. The advantage of this approach lies in its simplification of the multi-phase problem. Models employing the M^2 approach have until recently assumed isothermal conditions, [12]. In this paper the M^2 simplification is not used.

In contrast, very few transient models of PEMFC exist, despite the obvious transient nature of the cell operation in the primary application of powering automobiles. Um et al. developed a single-phase, isothermal 2D transient model in [16] and a similar 3D model in [17], though transient simulation results are not presented in the latter. 3D models can also be found in [18–21], none of which include liquid water transport and an energy balance—vital to describing flooding, membrane hydration and phase change. A more comprehensive one-dimensional model is presented in [22] in which liquid water is accounted for in a fully two-phase manner. However, the model is isothermal and in comparisons with potential sweep experiments it fails to capture the sensitive balance between flooding effects and membrane hydration. For a more detailed review of fuel cell modelling to 2004 we refer to [23].

The aim of this paper is to reproduce the phenomenon observed in the aforementioned experiments and those in [24] by developing a transient, non-isothermal model that explicitly incorporates the GDL, catalyst layers and membrane. In the present case, a one-dimensional formulation, based largely on our earlier work in [25], is shown to be sufficient to qualitatively capture observed behaviour – by comparison with [22,24] – and predict performance. Efforts to extend the model to two and three dimensions are ongoing.

2. Model assumptions and equations

The various features and assumptions that form the basis of our model are now listed.

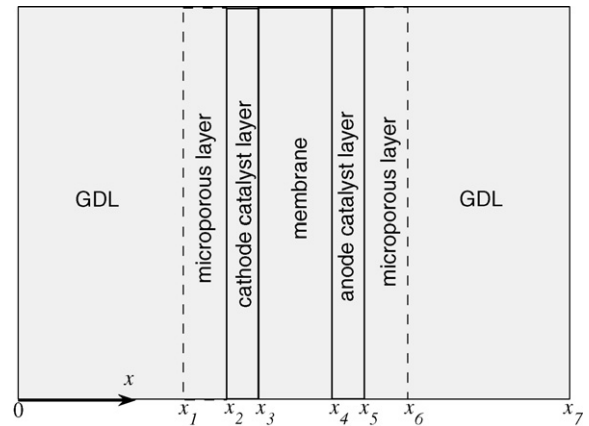


Fig. 1. Model geometry.

1. *One-dimensional full MEA transient.* The domain includes the entire membrane electrode assembly from the interface between the gas channels and GDL to the membrane (see Fig. 1). Each component is modelled explicitly. We allow for the inclusion of micro-porous layers between the GDL and catalyst layers. These layers serve two primary purposes: to prevent flooding in the catalyst layers and to decrease the contact resistance between the catalyst layer and diffusion medium [26,27].
2. *Catalyst layers.* We assume that the carbon support forms spherical clusters (agglomerates). Surrounding each agglomerate is an electrolyte layer, on which a layer of liquid water can also exist. We assume that the contact between the carbon agglomerates is sufficient to ensure the free flow of protons and electrons, and that the connecting paths possess a negligible volume fraction (a Bruggemann correction is used to account for the tortuosity of the flow paths). Within the agglomerates exists a fraction of the electrolyte, which we assume forms a negligible surface area of contact with any Pt that may also exist inside the agglomerates. It is possible to derive an effectiveness factor to remove this assumption. However, since it is unclear that significant reaction occurs within the agglomerates [28–31], an effectiveness factor is not employed. The pores between agglomerates are referred to as *primary pores*, distinct from the smaller pores between the carbon particles.
3. *Reactant transport.* Diffusion in the primary pores of the catalyst layers is assumed to be predominantly continuum, given their characteristic size and the typical operating pressures. Assuming that the oxygen and water vapour are small concentrations in a nitrogen gas, we employ Fick's law on the cathode side. On the anode side we assume the typical composition of hydrogen and vapour, with hydrogen the dominating component. The oxygen and hydrogen in the primary pores of the catalyst layers reach the Pt particles on the agglomerate surfaces by dissolving in the water/electrolyte and diffusing across the surrounding layers. Henry's law is used to describe the equilibrium in oxygen concentration at the interface between the gas and liquid/solid phases and mass is allowed to be exchanged freely at the surfaces. That is, the deviation from this equilibrium provides a driving

Table 1
Sources and sinks for the vapour equation (3)

	ACL	CCL	GDL/MPL	Meaning
S_{ce}	$-h_{pc}(X_{vP} - P_{sat})$	$-h_{pc}(X_{vP} - P_{sat})$	$-h_{pc}(X_{vP} - P_{sat})$	Condensation/evaporation
S_{ad}	$h_{dv}(C_d - C_d^*)$	$h_{dv}(C_d - C_d^*)$	0	H_2O^{liq}/H_2O^{dis} exchange

force for interfacial mass transfer, which occurs at a finite rate.

- Proton and electron concentration.** The protons are assumed to be transported in the form of hydronium ions, H_3O^+ . We explicitly model proton and electron transport through the ionomer, membrane, carbon support and GDL, assuming electro-neutrality. As in [16,32,22,20,21], we assume a pseudo steady state for the electron and proton transport/generation. The justification for this can be found in [20].
- Water.** The model accounts for water in all three forms; as a dissolved species, as vapour and as liquid. Liquid water resides in the primary pores. We assume that the net water produced is in dissolved form, consistent with the reaction location and the strongly hydrophilic nature of the ionomer. Condensation and evaporation are modelled using the approach in [2,4,5], and references therein. In this representation the transfer occurs at a finite rate, dictated by the deviation of the local thermodynamic state from equilibrium. In a similar fashion, we introduce phase change between vapour and dissolved water and between liquid and dissolved water by considering the deviation from an equilibrium between the phases. Details are presented later.
- Convective flow.** As in [5,22,33] the steady-state Darcy's law is employed for the convective flow of gas and liquid in the pores. This approach is also found in mining, hydrology and combustion literature [34], where a steady-state Darcy's law is a standard approximation.
- Temperature.** The model is non-isothermal, which is necessary to model phase change accurately and to study the effects of water activity. We do however assume a single temperature for all phases.

2.1. Gas phase equations

Let s denote liquid water (H_2O^{liq}) saturation, C_O , C_N , C_H and C_v , respectively the concentrations of oxygen, nitrogen, hydrogen and water vapour in the pore space, and $C_{i,e}$, $i \in \{O, H\}$, the concentrations of oxygen and hydrogen in the catalyst layer ionomer. The subscript j refers to anode (a) and cathode (c), and the subscript i refers to oxygen (O) and hydrogen (H). Taking into account reaction, diffusion and absorption, mass balances yield

$$\epsilon \frac{\partial}{\partial t} [(1-s)C_i] - \frac{\partial}{\partial x} \left(D_{p,i} \frac{\partial C_i}{\partial x} - v_g C_i \right) = -h_{pe,i}(H_i C_i - C_{i,e}) \quad (1)$$

$$\epsilon \frac{\partial}{\partial t} [(1-s)C_N] - \frac{\partial}{\partial x} \left(D_N \frac{\partial C_N}{\partial x} - v_g C_N \right) = 0 \quad (2)$$

$$\epsilon \frac{\partial}{\partial t} [(1-s)C_v] - \frac{\partial}{\partial x} \left(D_v \frac{\partial C_v}{\partial x} - v_g C_v \right) = S_{ce} + \nu S_{ad} \quad (3)$$

where $D_{p,i}$, D_N and D_v , $i \in \{O, H\}$, are the diffusion coefficients of oxygen, hydrogen, nitrogen and water vapour (H_2O^{vap}) through the GDL and primary pore of the catalyst layers. They are subject to a Bruggeman correction and their dependence on temperature and pressure follows the Chapman–Enskog formula [35], shown in Table 5. In these expressions T is temperature and P is the gas pressure. The porosity ϵ takes the value ϵ_p in the catalyst layers, ϵ_g in the GDL and ϵ_{mp} in the micro-porous layers.

The quantity v_g is the gas velocity, assumed to follow Darcy's law

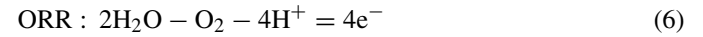
$$v_g = -\frac{\kappa}{\mu} (1-s)^3 \frac{\partial P}{\partial x}, \quad (4)$$

where κ is the permeability of the GDL, micro-porous or catalyst layers and μ is the dynamic viscosity of the gas. The permeability can be approximated by the Kozeny–Carman law,

$$\kappa = \frac{d^2}{K} \frac{\epsilon^3}{(1-\epsilon)^2}, \quad (5)$$

where d is a mean pore diameter and K is the so-called Kozeny–Carman constant. The two source terms in Eq. (3) are defined in Table 1.

The quantity $\nu = 1800 \text{ mol m}^{-3}$ is the fixed-charge site concentration of the membrane; $\mathcal{R}_j(\eta_j, T, C_{i,e}^s)$ are the reaction rates (based on the Butler–Volmer law); $h_{pe,i}$ is a volumetric mass transfer coefficient from gas to electrolyte (on the air side) and H_i is a dimensionless Henry constant. The reaction kinetics at the two electrodes can be summarized as follows:



We denote by ν_j , $j \in \{a, c\}$, the stoichiometric coefficients and by n the number of electrons transferred.

The diffusive flux of reactants from the pore space to the interface between the gas and electrolyte/water is balanced by the amount absorbed into the electrolyte/water. To prescribe the mass-transfer coefficient, $h_{pe,i}$, we use the formula for the Sherwood number given in [35] for flow past a spherical particle

$$Sh = 2 + 0.6 Re^{1/3} Sc^{2/3}, \quad (7)$$

where Re is the Reynolds number and Sc is the Schmidt number. For a predominantly diffusive process, we can approximate $Sh = 2$. From the formula $h_{pe,i}/s_a = Sh D_{p,i}/D$, where D is an average pore diameter and s_a is the specific surface area of the agglomerates, we obtain $h_{pe,i} = O(10^5)$ or greater. We point out that estimating mass transfer coefficients is far from a trivial exercise and a detailed discussion will not be attempted here.

Table 2
Sources and sinks for the dissolved reactants, potential and dissolved-water equations (10), (12) and (14)

	ACL	CCL	Membrane	GDL/MPL	Meaning
S_{ex}	$h_{pe,H}(H_H C_H - C_{H,e})$	$h_{pe,O}(H_O C_O - C_{O,e})$	0	–	Reactant absorption
S_r	$-\nu_a \mathcal{R}_a(\eta_a, T, C_{H,e}^s)/n$	$-\nu_c \mathcal{R}_c(\eta_c, T, C_{O,e}^s)/n$	0	–	Reactant depletion
S_ϕ	$-nFS_r/\nu_a$	$-nFS_r/\nu_c$	0	–	H_3O^+ source/sink
S_ψ	$-S_\phi$	$-S_\phi$	–	0	e^- source/sink
S_w	0	$\mathcal{R}_c(\eta_c, T, C_{O,e}^s)/(2\nu)$	0	–	Water production
S_{dl}	$h_{ld}(C_d - C_{d,1}^*)$	$h_{ld}(C_d - C_{d,1}^*)$	–	–	H_2O^{liq}/H_2O^{dis} exchange

2.2. Membrane and carbon phases

The electrolyte volume fraction, ϵ_e , will increase as the electrolyte swells with water. We separate the electrolyte film that coats the agglomerates (volume fraction ϵ_e^f) from that contained in the interiors (volume fraction ϵ_e^i) and write $\epsilon_e^0 = \epsilon_e^f + \epsilon_e^i$. The Pt inside the agglomerates is assumed to be inactive, that is, there is a negligible surface area of Pt in contact with the fraction ϵ_e^i of electrolyte. The combined volume fraction of the carbon, Pt and small pores, ϵ_a , is assumed constant. The volume fraction of primary pores is then given by $\epsilon_p = 1 - \epsilon_a - \epsilon_e$. The swelling of the electrolyte is assumed to impact on the thickness of the electrolyte film. To incorporate it we use the following approximate relationship

$$\epsilon_e = \epsilon_e^0 + k_s \lambda, \quad (8)$$

where $k_s = 0.0126$, and λ is the membrane water content (mol H_2O /mol SO_3^-), given by

$$\lambda = \frac{C_d}{1 - k_s C_d}, \quad (9)$$

where C_d is the dissolved water (H_2O^{dis}) concentration in the electrolyte, normalized with respect to (*i.e.*, divided by) ν .

The equations for reactant concentration in the ionomer and membrane are given by

$$\epsilon \frac{\partial C_{i,e}}{\partial t} - \frac{\partial}{\partial x} \left(\epsilon^{3/2} D_{e,i} \frac{\partial C_{i,e}}{\partial x} \right) = S_r + S_{ex}, \quad (10)$$

where $\epsilon = \epsilon_e$ in the catalyst layers and $\epsilon = 1$ in the membrane. Note that we use a Bruggeman correction. The diffusion coefficient of oxygen through the electrolyte has the following form (taken from [36])

$$D_{e,O} = 3.1 \times 10^{-7} e^{-2768/T}. \quad (11)$$

For hydrogen we use the constant value in Table 5.

To derive equations for the potentials in the membrane and carbon phases, ϕ and ψ respectively, we consider a mass balance for H_3O^+ and electrons, with the assumptions of electro-neutrality and steady-state

$$-\frac{\partial}{\partial x} \left(\epsilon^{3/2} \sigma_e \frac{\partial \phi}{\partial x} \right) - S_\phi = -\frac{\partial}{\partial x} \left(\epsilon^{3/2} \sigma_s \frac{\partial \psi}{\partial x} \right) + S_\psi = 0, \quad (12)$$

where σ_e and σ_s are the protonic and (effective) electronic conductivity respectively and F is Faraday's constant. Note that we have used a Bruggeman correction in both equations. $\epsilon = \epsilon_e$ in the catalyst layers and $\epsilon = 1$ in the membrane for the ionic

potential and $\epsilon = 1 - \epsilon_g$ ($\epsilon = 1 - \epsilon_{mp}$) in the GDL (MPL) and $\epsilon = \epsilon_c$ in the catalyst layers for the electronic potential. The source terms are given in Table 2.

For σ_e we use the law derived in [37],

$$\sigma_e = \exp \left(1286 \left(\frac{1}{303} - \frac{1}{T} \right) \right) (0.514\lambda - 0.326). \quad (13)$$

The algebraic term on the right-hand side of (13) accounts for the effect of hydration on the conductivity. It is based on empirical data collected by Springer et al. [37]. Values for σ_s have been discussed by Sun and Karan in [38]. To be consistent with their interpretation, we use the value $\sigma_s = 500 \text{ S m}^{-1}$.

The mass balance for water dissolved in the electrolyte is written as follows

$$\epsilon \frac{\partial C_d}{\partial t} - \frac{\partial}{\partial x} \left(\epsilon D_d \frac{\partial C_d}{\partial x} + \frac{5}{44F\nu} \lambda \epsilon \sigma_e \frac{\partial \phi}{\partial x} \right) = -S_{ad} + S_w - S_{dl}, \quad (14)$$

in which $\epsilon = 1$ for the membrane and $\epsilon = \epsilon_e$ for the catalyst layers. The term S_w represents water production and S_{dl} represents mass transfer between the liquid and dissolved phases (see Section 2.5). D_d is the diffusion coefficient for dissolved water [39]

$$\begin{aligned} D_d &= 3.1 \times 10^{-7} \lambda (e^{0.28\lambda} - 1) e^{-2436/T} \quad (0 < \lambda \leq 3), \\ D_d &= 4.17 \times 10^{-8} \lambda (1 + 161 e^{-\lambda}) e^{-2436/T} \quad (3 < \lambda \leq 22). \end{aligned} \quad (15)$$

The source term S_{ad} is defined in Table 1

2.3. Energy

An equation for the temperature, T , is derived from an energy balance of conduction, convective heat flux and heat sources

$$\begin{aligned} &\frac{\partial}{\partial t} (\epsilon s \rho_l C_l T + \epsilon (1-s) \rho_g C_g T + \rho_s C_s T) \\ &+ \frac{\partial}{\partial x} (\epsilon s \rho_l C_l T + \epsilon (1-s) \rho_g C_g T) - \frac{\partial}{\partial x} \left(k \frac{\partial T}{\partial x} \right) \\ &= S_{act} + S_{rev} + S_{ohm} + S_{pc}, \end{aligned} \quad (16)$$

where ρ_l (ρ_g) is the density of liquid water (the gas phase), C_l (C_g) is the specific heat capacity of liquid water (the gas phase), and k is the effective thermal conductivity, found from a volume average of the individual conductivities

$$k = k_p(1-s)\epsilon + k_e\epsilon_e + k_{ls}\epsilon_p + k_a\epsilon_a, \quad (17)$$

Table 3
Sources and sinks for the energy equation (16)

	Membrane	Catalyst layers	GDL/MPL	Meaning
S_{act}	0	$F\eta_j\mathcal{R}_j(\eta_j, T, C_{i,e}^s)$	0	Activation losses
S_{rev}	0	$-\Delta_j T\mathcal{R}_j(\eta_j, T, C_{i,e}^s)/n$	0	Heat of reaction
S_{ohm}	$\sigma_e(\partial\phi/\partial x)^2$	$\epsilon_e^{3/2}\sigma_e(\partial\phi/\partial x)^2 + \epsilon_c^{3/2}\sigma_s(\partial\psi/\partial x)^2$	$(1 - \epsilon_g/\epsilon_{mp})^{3/2}\sigma_s(\partial\psi/\partial x)^2$	Ohmic losses
S_{pc}	0	$h_{gl}h_{pc}(X_{vP} - P_{sat})$	$h_{gl}h_{pc}(X_{vP} - P_{sat})$	Heat of evaporation

where k_p , k_e , k_a and k_l are the thermal conductivities of the pore space, electrolyte, agglomerates (averaged) and liquid water respectively. In the GDL $\epsilon = \epsilon_g$, in the micro-porous layers $\epsilon = \epsilon_{mp}$ and in the catalyst layers $\epsilon = \epsilon_p$.

The quantity v_l is the liquid water interstitial velocity, which we define later. The source terms in equation (16) are defined in Table 3. In these expressions $-\Delta_j$ is the entropy associated with ORR ($j = c$) and HOR ($j = a$), h_{pc} is a mass transfer coefficient (defined below) and h_{gl} is the liquid–gas enthalpy change for water.

2.4. Liquid water

For liquid water, the mass balance is

$$\frac{\epsilon\rho_l}{W_1} \frac{\partial s}{\partial t} - \frac{\partial}{\partial x} \left(\frac{\epsilon_p\rho_l}{W_1} v_l \right) = S_{ce} + \nu S_{dl}, \quad (18)$$

where the source terms, defined in Tables 1 and 2, represent condensation/evaporation and interfacial mass transfer between the liquid and dissolved phases (the last term on the right-hand side is explained and discussed in Section 2.5). W_1 is the molar mass of liquid water, $\epsilon = \epsilon_g$ in the GDL, $\epsilon = \epsilon_{mp}$ in the micro-porous layers and $\epsilon = \epsilon_p$ in the catalyst layers. v_l is determined by the Darcy-law approximation to momentum conservation

$$v_l = \frac{\kappa_l}{\mu_l} \frac{\partial p}{\partial x}, \quad (19)$$

where κ_l , μ_l and p are respectively the relative permeability, viscosity and pressure of the liquid.

A great deal of debate surrounds both the form and magnitude of the permeability and capillary pressure. Mazumder [4], compares the Leverette model employed in [9] with the empirical relationship in [5], in which both of these quantities assume entirely different forms, yielding markedly different predicted levels of saturation. There are also other models of liquid transport in porous media, of varying degrees of sophistication. For example, Nam and Kaviani [40], scale saturation against an immobile value (below which the liquid water is discontinuous and therefore does not move), and place the scaled saturation inside the Leverette function. All of the forms mentioned can be easily implemented in our model but, in the absence of conclusive experimental data, we choose to follow the most widely employed form, found in [9].

The liquid pressure is given as the difference between the gas and capillary pressures

$$p = P - p_c, \quad (20)$$

so that differentiating Eq. (18) and using Eq. (19) yields

$$\frac{\epsilon\rho_l}{W_1} \frac{\partial s}{\partial t} - \frac{\rho_l}{\mu_l W_1} \frac{\partial}{\partial x} \left(\epsilon\kappa_l(s) \left[-\frac{dp_c}{ds} \frac{\partial s}{\partial x} + \frac{\partial P}{\partial x} \right] \right) = S_{ce} + \nu S_{dl}, \quad (21)$$

In the catalyst layers the capillary pressure and permeability are defined as

$$p_c = \sigma_c \mathcal{J}(s), \quad \kappa_l(s) = \kappa_c s^3, \quad (22)$$

where κ_c is the absolute permeability of the catalyst layers and $\mathcal{J}(s)$ is the Leverette function. The quantity σ_c is defined as follows

$$\sigma_c = \sigma' \cos \theta_c^j \sqrt{\frac{\epsilon_p}{\kappa_c}}, \quad (23)$$

where θ_c^j is the contact angle for the catalyst layers ($0 < \theta_c^j < \pi/2$) and σ' is the surface tension. The grouping $2\sqrt{\epsilon_p/\kappa_c}$ is then equal to the characteristic capillary radius.

The Leverette function for a hydrophilic medium, for which the wetting phase is the liquid, is given by

$$\mathcal{J}(s) = 1.417(1 - s) - 2.12(1 - s)^2 + 1.262(1 - s)^3. \quad (24)$$

In the GDL and micro-porous layers

$$p_c = \sigma_g \mathcal{J}(s), \quad \kappa_l(s) = \kappa_g s^3, \quad \sigma_g = \sigma' \cos \theta_c^g \sqrt{\frac{\epsilon_g}{\kappa_g}},$$

$$p_c = \sigma_{mp} \mathcal{J}(s), \quad \kappa_l(s) = \kappa_{mp} s^3, \quad \sigma_{mp} = \sigma' \cos \theta_c^{mp} \sqrt{\frac{\epsilon_{mp}}{\kappa_{mp}}}, \quad (25)$$

where κ_g (κ_{mp}) is the absolute permeability of the GDL (micro-porous layer) and θ_c^g (θ_c^{mp}) is the contact angle ($\pi/2 < \theta_c^g < \pi$). The Leverette function for a hydrophobic medium, for which the wetting phase is the gas phase, is given by

$$\mathcal{J}(s) = 1.417s - 2.12s^2 + 1.262s^3. \quad (26)$$

The liquid–vapour phase-change term, derived from that given in [4] and references therein, is driven by the deviation from equilibrium, $RTC_v - P_{sat}$, where P_{sat} is the saturation pressure of water and the first term is equivalent to the partial pressure of the vapour. The latter is defined by $X_v P$, where P is the pressure of the gas phase and X_v is the molar fraction of vapour. Using the ideal gas law, $P = CRT$, X_v is given by

$$X_v = \frac{C_v}{C} = \frac{C_v RT}{P}, \quad (27)$$

where $C = C_v + C_N + C_i$ is the molar density of the gas ($i = O$ at the cathode and $i = H$ in the anode). A relationship for the

saturation pressure is provided in the discussion of the boundary conditions. In order to distinguish between evaporation and condensation, the mass-transfer coefficient h_{pc} depends on the sign of the driving force $X_{vP} - P_{sat}$ and its precise form is

$$h_{pc} = \begin{cases} k_c \frac{\epsilon_p(1-s)X_v}{RT} & X_{vP} > P_{sat} \\ k_e \frac{\epsilon_p s \rho_l}{W_1} & X_{vP} < P_{sat} \end{cases}, \quad (28)$$

where k_c and k_e are the condensation and evaporation rate constants, whose values are taken from [2]. We use a continuously-differentiable implementation of the following form

$$h_{pc} = \frac{k_c \epsilon_p (1-s) X_v}{2RT} \left(1 + \frac{|X_{vP} - P_{sat}|}{X_{vP} - P_{sat}} \right) + \frac{k_e \epsilon_p s \rho_l}{2W_1} \left(1 - \frac{|X_{vP} - P_{sat}|}{X_{vP} - P_{sat}} \right). \quad (29)$$

In a similar fashion, the vapour-dissolved phase-change term in Eqs. (3) and (14) is driven by the deviation from equilibrium between the vapour and dissolved water, $C_d - C_d^*$, where C_d^* is the dissolved concentration at equilibrium. The latter is derived from the following law for the equilibrium water content measured at 80 °C (found in [41])

$$\lambda^* = 0.3 + 10.8a_w - 16a_w^2 + 14.1a_w^3, \quad C_d^* = \frac{\lambda^*}{1 + 0.0126\lambda^*}, \quad (30)$$

where a_w is the water vapour activity. To distinguish between desorption and water-uptake of the electrolyte (adsorption), the mass-transfer coefficient h_{dv} depends on the sign of the driving force $C_d - C_d^*$. From the experimental and numerical results in [42], we can approximate the coefficients of absorption and desorption as follows

$$h_{dv} = \begin{cases} \kappa_a(1-s)\lambda & C_d - C_d^* < 0 \\ \kappa_d(1-s)\lambda & C_d - C_d^* > 0 \end{cases}, \quad (31)$$

where κ_d and κ_e are given in Table 4. Their weak dependence on temperature variations is neglected. The factor $1 - s$ accounts for the blockage of the pores by the liquid water. To implement this approach we use a continuously differentiable form of

$$h_{dv} = \frac{1}{2}\kappa_d(1-s)\lambda \left(1 + \frac{|C_d - C_d^*|}{C_d - C_d^*} \right) + \frac{1}{2}\kappa_a(1-s)\lambda \left(1 - \frac{|C_d - C_d^*|}{C_d - C_d^*} \right), \quad (32)$$

2.5. Liquid-dissolved water mass transfer and Schroeder's paradox

It is well known that the water content λ depends on the water activity, $a_w = X_v P / P_{sat}$. The precise relationship was correlated by Hinatsu et al. in [41],

$$\lambda = \lambda_v = 0.3 + 10.8a_w - 16a_w^2 + 14.1a_w^3 \quad (\text{at } 353 \text{ K}), \quad (33)$$

which has a maximum of $\lambda_v = 9.1$ at equilibrium with vapour. However, when the electrolyte is submerged in liquid water its

equilibrium water content appears to jump discontinuously to a higher value, given in the following

$$\lambda = 22 \quad \text{or equivalently} \quad C_d = C_{d,1}^* = \frac{22}{1 + 22k_s}, \quad (34)$$

as dictated by Eq. (9). In an attempt to capture this anomaly, known as Schroeder's paradox, we introduce the mass-transfer term S_{dl} in Eqs. (14) and (18), defined in Table 2. This term is decomposed into separate terms for absorption and desorption of liquid water to and from the ionomer in the catalyst layers. When the liquid-equilibrated water content value $C_{d,1}^*$ is reached, it is assumed that desorption of water from the ionomer as a liquid takes place, the magnitude of which is driven by the deviation of C_d from $C_{d,1}^*$. The desorption part of the term in Table 2 therefore takes the form

$$h_{des} = \frac{1}{2}k_{des} \left(1 + \frac{|C_d - C_{d,1}^*|}{C_d - C_{d,1}^*} \right). \quad (35)$$

where k_{des} is the coefficient of desorption and could itself depend on saturation and water content but for simplicity is assumed to be constant.

In addition we introduce an absorption term that represents, in its presence, the uptake of liquid water by the ionomer, the magnitude of which is again assumed to be proportional to the deviation of C_d from $C_{d,1}^*$. However, it is further assumed that the liquid water droplets are not contiguous until the *immobile saturation*, s_* , is reached (by definition of the immobile saturation). By this approximation we are equivalently assuming that at $s = s_*$ the agglomerates are entirely coated with liquid water and equilibrium can be achieved. We use the value of $s_* = 0.1$ given in [40], and refer to that paper for references related to its measurement. The absorption term therefore takes the form

$$h_{ads} = \frac{1}{2}k_{ads} \left(1 + \frac{|s - s_*|}{s - s_*} \right) \times \frac{1}{2} \left(1 - \frac{|C_d - C_{d,1}^*|}{C_d - C_{d,1}^*} \right). \quad (36)$$

where k_{ads} is the coefficient of absorption, which, for simplicity, is assumed to be constant. Notice that the last term in brackets in (36) is zero when $C_d > C_{d,1}^*$ so that it does not contribute to desorption. The mass transfer term in Table 2 is therefore defined as follows

$$h_{dl} = \frac{k_{ads}}{4} \left(1 + \frac{|s - s_*|}{s - s_*} \right) \left(1 - \frac{|C_d - C_{d,1}^*|}{C_d - C_{d,1}^*} \right) + \frac{k_{des}}{2} \left(1 + \frac{|C_d - C_{d,1}^*|}{C_d - C_{d,1}^*} \right) \quad (37)$$

Again this is implemented in a continuously differentiable form to prevent the occurrence of singularities in the numerical computations.

The values of k_{ads} and k_{des} are chosen large enough that if C_d approaches $C_{d,1}^*$ its value does not overshoot it significantly (as with the treatment of condensation and evaporation). These values are given in Table 5. A list of other parameters and their values can also be found in Tables 4 and 5.

Table 4
Parameter values used in the base case calculations

Symbol	Quantity	Size	References
Structural			
L	Catalyst layer thickness	25 μm	
L_m	Membrane thickness	50 μm	
L_{mp}	GDL + MPL total thickness	200 μm	
L_G	MPL thickness	30 μm	
ϵ_e^i	Electrolyte volume fraction in agglomerates	0.2	[30]
ϵ_a	Volume fraction of agglomerates	0.4215	[30]
ϵ_c	Volume fraction of carbon in catalyst layers	0.2	
ϵ_g	Porosity of the GDL	0.74	[47]
ϵ_{mp}	Porosity of micro-porous layer	0.3	[47]
R_{ag}	Agglomerate radius	0.2 μm	[30]
δ_0^e	Electrolyte film thickness w/o swelling	15 nm	[48]
N	Agglomerate density	$1.257 \times 10^{19} \text{ m}^{-3}$	est.
a_{pt}	Specific surface area of Pt	$1000 \text{ cm}^2 (\text{mg Pt})^{-1}$	[49]
m_{pt}	Pt loading	$0.4 (\text{mg Pt}) \text{ cm}^{-2}$	[3]
$\theta_c^j (\theta_c^g)$	Catalyst-layer (GDL) contact angle	$90^\circ (120^\circ)$	[50]
d_g, d_{mp}, d_c	GDL, MPL, catalyst-layer pore size	10 μm , 1 μm , 2 μm	
Electrochemical			
$i_{\text{ref},i}$	Cathode (anode) exchange current density	$10^{-3} (10^3) \text{ A m}^{-2}$	[51]
$C_{\text{ref},i}$	Reference O_2 (H_2) concentration	0.005 (0.02) mol m^{-3}	[51]
α_c	Cathodic transfer coefficient	0.55	
α_a	Anodic transfer coefficient	0.45	
E_0	Open circuit potential	0.95 V	
$-\Delta_c$	Entropy associated with ORR	$163.7 \text{ J mol}^{-1} \text{ K}^{-1}$	[52]
$-\Delta_a$	Entropy associated with HOR ²	$0 \text{ J mol}^{-1} \text{ K}^{-1}$	[52]
Channel conditions			
$T_c (T_a)$	Cathode (anode) channel temperature	60 $^\circ\text{C}$ (60 $^\circ\text{C}$)	
$a_{w,c} (a_{w,a})$	Cathode (anode) channel water activity	0.8 (0.8)	
$\bar{C}_c (\bar{C}_a)$	Cathode (anode) channel gas concentration	$P_c/RT_c (P_a/RT_a) \text{ mol m}^{-3}$	
$\bar{C}_{O,c}$	Oxygen concentration in cathode channel	$0.21(\bar{C}_c - \bar{C}_{v,c}) \text{ mol m}^{-3}$	
$\bar{C}_{H,a}$	Hydrogen concentration in anode channel	$(\bar{C}_a - \bar{C}_{v,a}) \text{ mol m}^{-3}$	
$P_c (P_a)$	Gas pressure in the cathode (anode) channel	30 psig (206.842 kPa)	
$\bar{C}_{v,c}$	Vapour concentration in cathode channel	$RT_c P_{\text{sat},c} \bar{C}_c / P_c \text{ mol m}^{-3}$	
$\bar{C}_{v,a}$	Vapour concentration in anode channel	$RT_a P_{\text{sat},a} \bar{C}_a / P_a \text{ mol m}^{-3}$	
Ω_j	Liquid water removal constants	0.075 m^{-1}	

2.6. Reaction rate and limiting current density

The reaction rates (in $\text{mol m}^{-3} \text{ s}^{-1}$) are given by the Butler–Volmer law and first-order kinetics in reactant concentration

$$\mathcal{R}_j(\eta_j, T, C_{i,e}^s) = \frac{a i_{\text{ref},i}}{FC_{\text{ref},i}} \epsilon_e C_{i,e}^s (e^{\alpha_a F \eta_j / RT} - e^{-\alpha_c F \eta_j / RT}), \quad (38)$$

where $i = \text{O}$ and $j = \text{c}$ or $i = \text{H}$ and $j = \text{a}$. The quantities $i_{\text{ref},i}$ are the cathode and anode exchange current densities, α_a and α_c are the anodic and cathodic transfer coefficients, $C_{\text{ref},i}$ are the reference reactant molar concentrations, a is the volumetric specific surface area of catalyst (per unit volume of catalyst layer), η_j , $j \in \{\text{a,c}\}$, is the overpotential and R is the universal gas constant ($8.314 \text{ J mol}^{-1} \text{ K}^{-1}$). The quantity a is a function of the mass specific Pt surface area (Pt surface area per unit mass of Pt), a_{pt} , the Pt loading, m_{pt} , and the catalyst-layer thickness, L

$$a = \frac{a_{\text{pt}} m_{\text{pt}}}{L}.$$

The overpotentials, η_j , are defined precisely through the relationships

$$\eta_c = \psi - \phi - E_0, \quad \eta_a = \psi - \phi, \quad (39)$$

where E_0 is the so-called open circuit potential, assumed constant. The value of reactant concentrations in the Butler–Volmer expression, (38), ought to reflect accurately that reaction takes place at the surfaces of the carbon agglomerates. The concentrations at these surfaces, $C_{i,e}^s$, $i \in \{\text{O, H}\}$, are generally different from the bulk values in the electrolyte, particularly given the restricted diffusion of reactants. The $C_{i,e}^s$ can be related to the bulk values, $C_{i,e}$, by balancing the rate of reaction with the rate of diffusion of reactant to the surface of the agglomerates (at steady state). This mass balance can be approximated as follows

$$\gamma(C_{i,e} - C_{i,e}^s) = \frac{v_j}{n} \mathcal{R}_j(\eta_j, T, C_{i,e}^s), \quad (40)$$

where γ is the rate of oxygen diffusion through the electrolyte/water film to the surface of the agglomerates (in s^{-1}). Using the definition of $\mathcal{R}_j(\eta_j, T, C_{i,e}^s)$ and solving the resulting

Table 5
Heat, charge and mass transfer/transport properties in the base case

Symbol	Quantity	Size	References
$D_{p,O}$	Oxygen diffusivity in free space	$3.8 \times 10^{-9} (\epsilon(1-s)T)^{3/2}/P \text{ m}^2 \text{ s}^{-1}$	[35]
$D_{p,H}$	Hydrogen diffusivity in free space	$10^{-9} (\epsilon(1-s)T)^{3/2}/P \text{ m}^2 \text{ s}^{-1}$	[35]
D_v	Vapour diffusivity in free space	$4.1 \times 10^{-9} (\epsilon(1-s)T)^{3/2}/P \text{ m}^2 \text{ s}^{-1}$	[35]
D_N	Nitrogen diffusivity in free space	$3.6 \times 10^{-9} (\epsilon(1-s)T)^{3/2}/P \text{ m}^2 \text{ s}^{-1}$	[35]
D_l	Oxygen diffusivity in liquid water (60 °C)	$4.82 \times 10^{-9} \text{ m}^2 \text{ s}^{-1}$	[35]
$D_{e,H}$	Hydrogen diffusivity in nafion	$1 \times 10^{-10} \text{ m}^2 \text{ s}^{-1}$	
$h_{pe,j}$	Oxygen mass transfer rate	10^5 s^{-1}	est.
$H_O H_H$	O ₂ (H ₂) Henry's law constant (dimensionless)	0.3 (0.6)	[53]
$\kappa_a (\kappa_d)$	Absorption (desorption) constant	$10^{-5}/9 (10^{-5}/3) \text{ m s}^{-1}$	[2]
$\kappa_j (\kappa_g)$	Absolute permeability of CCL (GDL)	$10^{-13} (8.7 \times 10^{-12}) \text{ m}^2$	[54,47]
μ_l	Liquid water viscosity	$10^{-3} \text{ kg m}^{-1} \text{ s}^{-1}$	[4]
σ'	Surface tension	0.07 N m^{-1}	[4]
k	Thermal conductivity of catalyst layers	$0.67 \text{ W m}^{-1} \text{ K}^{-1}$	[51]
k_m	Thermal conductivity of membrane	$0.67 \text{ W m}^{-1} \text{ K}^{-1}$	[51]
k_G	Thermal conductivity of GDL	$1.67 \text{ W m}^{-1} \text{ K}^{-1}$	[51]
$\rho_l C_l$	Heat capacitance of water	$4.187 \times 10^6 \text{ J m}^{-3} \text{ K}^{-1}$	
$\rho_g C_g$	Heat capacitance of air	$10^3 \text{ J m}^{-3} \text{ K}^{-1}$	
$\rho_m C_m$	Heat capacitance of membrane	$2.18 \times 10^6 \text{ J m}^{-3} \text{ K}^{-1}$	
$\rho_c C_c$	Heat capacitance of carbon	$1.61 \times 10^6 \text{ J m}^{-3} \text{ K}^{-1}$	
$-\Delta_c$	Entropy associated with ORR	$163.7 \text{ J mol}^{-1} \text{ K}^{-1}$	[52]
$-\Delta_a$	Entropy associated with HOR ²	$0 \text{ J mol}^{-1} \text{ K}^{-1}$	[52]
σ_s	Electronic conductivity before correction	500 S m^{-1}	[38]
k_{des}	H ₂ O ^{liq} desorption coefficient	100 s^{-1}	
k_{ads}	H ₂ O ^{dis} adsorption coefficient	10 s^{-1}	

equation for $C_{i,e}^s$ then yields

$$C_{i,e}^s = \frac{\gamma C_{i,e}}{\gamma + \epsilon_e r (e^{\alpha_a F \eta_j / RT} - e^{-\alpha_c F \eta_j / RT})}, \quad \text{where} \quad (41)$$

$$r = \frac{\nu_j a i_{ref,i}}{n F C_{ref,i}},$$

so that the final form of the reaction rate is

$$\mathcal{R}_j(\eta_j, T, C_{i,e}^s) \equiv \mathcal{R}_j(\eta_j, T, C_{i,e})$$

$$= \frac{n \gamma \epsilon_e r C_{i,e} (e^{\alpha_a F \eta_j / RT} - e^{-\alpha_c F \eta_j / RT})}{\nu_j \gamma + \epsilon_e r (e^{\alpha_a F \eta_j / RT} - e^{-\alpha_c F \eta_j / RT})}. \quad (42)$$

In order to relate the diffusion rate γ to the microscopic properties of the catalyst layers, we define an electrolyte film thickness, δ_e , an agglomerate radius, R_{ag} , and the number of agglomerates per unit volume, N

$$\gamma(C_{i,e} - C_{i,e}^s) \approx A \times \underbrace{\frac{D_{e,i}}{\delta_e} (C_{i,e} - C_{i,e}^s)}_{\text{molar flux}}, \quad \text{so that } \gamma = \frac{A D_{e,i}}{\delta_e}, \quad (43)$$

where A is the specific surface area of agglomerates (we assume that all of the surface area is covered, whereupon $A = 4\pi R_{ag}^2 N$). The volume of electrolyte attached to the surface of each agglomerate is ϵ_e^f / N , which, from our assumptions, covers the entire surface of the agglomerate. The thickness δ_0^e (without swelling) and ϵ_e^f are therefore related as follows

$$\delta_0^e = \left(R_{ag}^3 + \frac{3\epsilon_e^f}{4\pi N} \right)^{1/3} - R_{ag} \quad (44)$$

The electrolyte swelling results in a volume change equal to (per agglomerate) $(\epsilon_e^f - \epsilon_0^f) / N$. The electrolyte film thickness is then given by

$$\delta_e = \left((R_{ag} + \delta_0^e)^3 + \frac{3(\epsilon_e^f - \epsilon_0^f)}{4\pi N} \right)^{1/3} - R_{ag}. \quad (45)$$

When $s > s_*$, as previously defined, the liquid water present in the catalyst layers will provide additional resistance to the oxygen, with a different diffusion coefficient D_l . Assuming that the electrolyte is hydrophilic, any liquid water is taken to coat the entire surface of the agglomerates. Based on these assumptions, the thickness of the water layer is given by

$$\delta_l = \left((R_{ag} + \delta_e)^3 + \frac{3s\epsilon_p}{4\pi N} \right)^{1/3} - (R_{ag} + \delta_e), \quad (46)$$

with a total film thickness (electrolyte and water)

$$\delta = \delta_e + \delta_l \quad (47)$$

The quantity γ then has to be modified; it is decomposed into a term arising from diffusion through the water layer, γ_l , and a term of the type described above, γ_e . To approximate the concentration of reactant at the agglomerate surfaces two balances need to be performed, one for diffusion through the water, to relate the bulk concentration to concentration at the water/electrolyte interface, and one between diffusion through the electrolyte and reaction, to relate the latter concentration to $C_{i,e}^s$. The reaction rate then takes the form (42) with

$$\gamma = \frac{\gamma_l \gamma_e}{\gamma_l + \gamma_e}, \quad \text{where } \gamma_l = \frac{A' D_l}{\delta_l}, \quad \gamma_e = \frac{A D_{e,i}}{\delta_e}, \quad (48)$$

$$A' = 4\pi (R_{ag} + \delta_e)^2 N.$$

The Henry constant H_i would likewise require modification. For oxygen, it is approximately 0.3 for water under typical operating conditions, and was assigned the value 0.15 for Nafion in [16]. However, given the uncertainty in its value we assume that the water value holds throughout, both for oxygen and hydrogen.

Note that the quantity N is a function of both the radius of the agglomerates and their distribution, for example, the more densely packed the agglomerates the larger N .

The current flow is the H_3O^+ flow, so that the current density, I' (in $A\ m^{-2}$), is given by integrating the volumetric value across the CCL

$$I' = 4Fr \int_{x_2}^{x_3} \frac{\gamma \epsilon_e C_{i,e} (e^{\alpha_a F \eta_j / RT} - e^{-\alpha_c F \eta_j / RT})}{\gamma + \epsilon_e r (e^{\alpha_a F \eta_j / RT} - e^{-\alpha_c F \eta_j / RT})} dx. \quad (49)$$

2.7. Initial and boundary conditions

For the discussion of the boundary conditions we recall Fig. 1. At the interface between the membrane and catalyst layers, $x = x_3$ and $x = x_4$, the gas phase fluxes are taken to be zero; that is, the gas species are assumed not to penetrate the pore space in the membrane. Similarly, we assume that the fluxes of reactants in the ionomer phase at the interfaces between the catalyst and gas-diffusion (or micro-porous) layers, $x = x_2$ and $x = x_5$, are small, *i.e.*, that the reactants enter predominantly through the gas phase and that mass exchange becomes significant in the catalyst layers. Since protons and dissolved species (reactants and water) have no effective transport mechanism in the gas-diffusion (or micro-porous) layers, their fluxes at these interfaces are taken to be zero.

$$\frac{\partial C_{i,e}}{\partial x} = \frac{\partial \phi}{\partial x} = D_d \frac{\partial C_d}{\partial x} + \frac{5}{44 F v} \lambda \sigma_e \frac{\partial \phi}{\partial x} = 0, \quad x = x_2, x_5 \quad (50a)$$

$$\frac{\partial C_i}{\partial x} = 0, \quad i \in \{O, H, N, v\}, \quad x = x_3, x_4 \quad (50b)$$

At the interfaces between the channels and GDL, the gas concentrations and temperature are prescribed, with oxygen only at the cathode side and hydrogen only at the anode side. The cell voltage, U_c , is measured at the cathode channel/GDL interface, and at the anode channel/GDL interface we assume a zero concentration of electrons.

$$C_i(0) = \bar{C}_{i,c} \quad (i \in \{O, N, v\}), \quad C_i(x_7) = \bar{C}_{i,a} \quad (i \in \{H, N, v\}), \\ \psi(0) = U_c, \quad \psi(x_7) = 0, \quad T(0) = T_c, \quad T(x_7) = T_a. \quad (50c)$$

The values of $\bar{C}_{v,c}$ and $\bar{C}_{v,a}$ are calculated from the water activity in the channels, $a_{w,c}$ and $a_{w,a}$ (for cathode and anode respectively). For the cathode, the activity is defined as $\bar{X}_{v,c} P_c / P_{sat}$, where $\bar{X}_{v,c}$ is the molar fraction of vapour in the cathode channel, P_c is the cathode-channel gas pressure and $P_{sat,c}$ is the cathode-channel saturation pressure. The saturation pressure, a function of temperature, is given by the formula in [37]

$$\log_{10} P_{sat} = -2.1794 + 0.02953(T - 273) - 9.1837 \\ \times 10^{-5}(T - 273)^2 + 1.4454 \times 10^{-7}(T - 273)^3. \quad (50d)$$

From these relationships we derive $\bar{C}_{v,c}$ in the cathode as follows

$$\bar{C}_{v,c} = \frac{RT_c P_{sat,c}}{P_c} \bar{C}_c, \quad (50e)$$

where \bar{C}_c is the total gas molar concentration in the cathode channel, calculated from the cathode-channel pressure and temperature

$$\bar{C}_c = \frac{P_c}{RT_c}. \quad (50f)$$

The same procedure is applied at the anode channel.

The final boundary condition is that for the liquid water at the interfaces between the gas channels and the GDL. It is common in modelling studies, for example [7,6,5,3], to assume either a zero saturation or zero liquid water flux at this location, or along portions of the channel/GDL interface in two dimensions. In the approach of Weber and Newman [43] the liquid water flux is assumed zero if the gas pressure is greater than the liquid pressure, otherwise the capillary pressure is assumed zero. However, as with the zero flux conditions, this implicitly assumes that the strength of the flow in the channel has no impact on the liquid water levels at the GDL surface. In [44] Meng and Wang specify the saturation at the GDL/channel interface, which, as they correctly state, depends sensitively on the gas flow in the channel, current density and wettability [45].

The accumulation and removal of liquid water along the channel is a complicated process. Water is expelled from the GDL through preferential openings and forms droplets attached to the surface. These droplets can grow or coalesce to a form larger droplets comparable in size to the channel dimensions, which results in the formation of a liquid film [46]. Ultimately, the film is wicked along the channel walls toward the exit. The greater the flow velocity in the channel, the more effective the removal of liquid water. A detailed model of this process, accounting for the surface properties of the GDL, phase change, surface tension, two dimensional gas flow and hydrophilicity of the channel walls, is not currently possible. To approximate the physics at the interfaces we adopt the following steady-state flux condition at $x = 0$ and $x = x_7$

$$\frac{\partial s}{\partial x} - \Omega_j s = 0, \quad j \in \{a,c\}, \quad (50g)$$

where $\Omega_j = 0$ corresponds to zero water removal from the anode channel, $j = a$, or cathode channel, $j = c$. This form is motivated in two ways. Firstly, there should be no removal at zero saturation. Secondly, the parameter Ω_j can be seen naturally as (in an average sense) the reciprocal of a water film thickness on the surface of the GDL. When this thickness approaches zero, the saturation is physically zero, which is expressed by $1/\Omega_j \rightarrow 0$ in Eq. (50g). The thickness, and therefore Ω_j , is likely to depend sensitively on the flow rate in the channel [46].

Initial conditions for pressure, temperature and vapour concentrations will typically be given by the ambient conditions in the channels. The water content of the membrane/ionomer is assumed to be given by equilibrium with vapour in the channels. The saturation at startup is assumed zero.

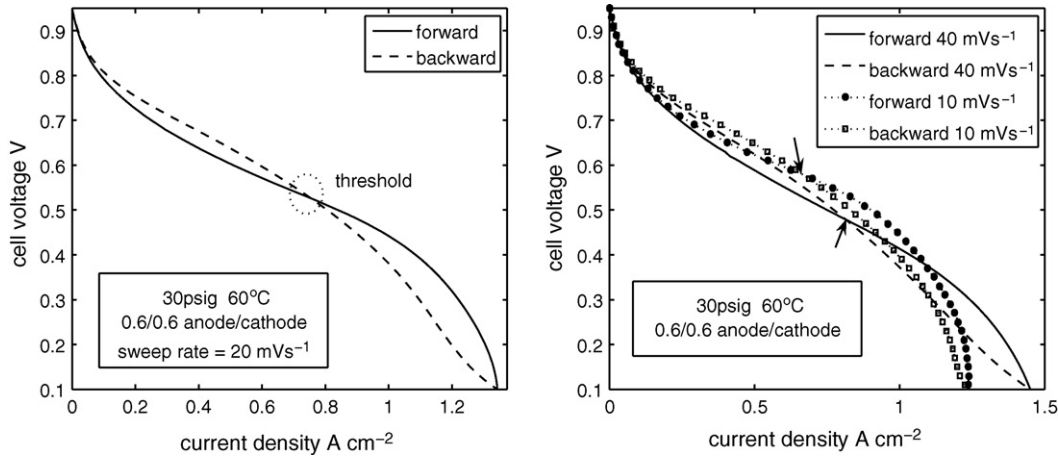


Fig. 2. The left-hand figure shows polarization curves generated from a sweep cycle at 20 mV s^{-1} using the parameter values in Tables 4 and 5, with no micro-porous layer. See Fig. 3 for profiles of saturation and membrane water content during the sweep cycle. In the right-hand figure the effect of the sweep rate is illustrated, with arrows indicating the locations of the thresholds.

2.8. Numerical details

The governing equations and boundary conditions laid out above were solved using the finite-element method implemented in COMSOL 3.2a. The discretization of the equations and boundary conditions was achieved on a uniform grid using quartic Lagrange polynomials as trial and test functions, allowing the number of grid points to be kept small (typically 64 or 128). The switch functions were substituted with hyperbolic tanh functions to smooth the discontinuities, a standard procedure.

The default set of parameter values used for the base case is given in Tables 4 and 5. No fitting parameters were used since we are interested in a qualitative picture of the behaviour. It would be possible through a single fitting of one or more parameters, such as exchange current density or platinum specific surface area (whose values are in any case highly uncertain), to obtain a closer quantitative match, but there is no loss of information in not doing so.

3. Results and discussion

3.1. Validation and sweep rate effect

To validate the model we make use of the results in [24] of ramp sweeps experiments in potentiostatic and galvanostatic mode. We attempt to capture the observed trends with specific examples of the effects on performance of the channel conditions and sweep rate. We then discuss results relating to certain microstructural properties of the gas-diffusion and micro-porous layers.

The very small active MEA area (1 cm^2) and high flow rates ($200\text{--}400 \text{ mL min}^{-1}$) in the experimental study in [24] ensured that the cell behaviour was very close to one-dimensional. The cell was conditioned with humidified hydrogen and air before switching to dry gases. In our results we shall consider a continuous input of partly humidified gases; simulation of the precise conditions is possible but the details of the humidification process are not provided in [24]. Moreover, a qualitative match

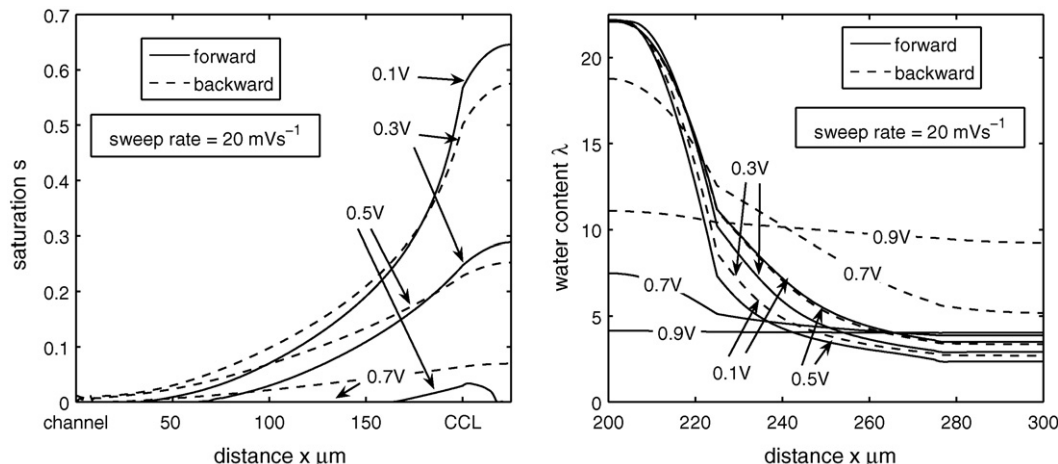


Fig. 3. Profiles of saturation in the cathode and membrane water content at selected moments during the forward and backward sweeps corresponding to Fig. 2 with a sweep rate of 20 mV s^{-1} . The corresponding voltages are indicated.

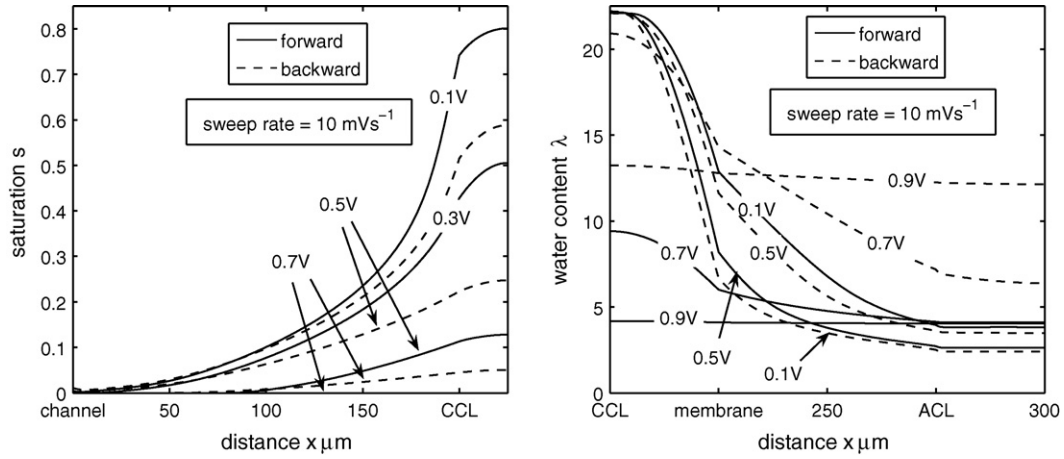


Fig. 4. Profiles of saturation in the cathode and membrane water content at selected moments during the forward and backward sweeps corresponding to the example with 10 mV s^{-1} in Fig. 2.

is achieved even with the continuously humidified input. Note finally that in [22], in which the same experimental procedure is presented and modelled, the authors fail to capture the most striking feature of a crossing of the polarization curves generated from the backward and forward sweeps in potentiostatic mode (to be discussed next). This phenomenon is illustrated in Fig. 1 of [24] and demonstrated in the many examples in both papers.

We refer first to Fig. 2, which demonstrates the polarization curve for the base-case parameters in Tables 4 and 5, without a micro-porous layer. What is immediately striking in this plot is the intersection of the curves at approximately 0.75 A cm^2 (0.55 V), marking the boundary between worse performance on the backward sweep for cell voltage below the value at the crossing point, and better performance for cell voltage above this value—compare this figure with the experimentally generated potentiostatic curves in [24,22].

To explain the trend we now refer to Fig. 3, showing the evolution of the membrane/ionomer water content and the saturation in the cathode at selected times during the sweep cycle. The corresponding voltages at these times are indicated. It is clear that during the backward sweep the saturation level is greater at each cell voltage value, a likely consequence of the different time

scales associated with evaporation and condensation. The mass transport limitations arising from the presence of liquid water are therefore more strongly felt at low cell voltage, as indicated in Fig. 2. However, once the mass transport limitations are overcome (the polarization curve enters the so-called ohmic regime) the greater saturation level of the backward sweep lowers the membrane resistance, in relation to the forward sweep.

Fig. 2 further shows polarization curves for the base case parameters with sweep rates of 10 and 40 mV s^{-1} , demonstrating that an increase in sweep rate moves the threshold cell voltage to a lower value and threshold current density to a higher value. These results are qualitatively very similar to Figs. 3 and 4 of [24], with a slight discrepancy in comparison to the former figure; the thresholds for 5 – 10 mV s^{-1} in Fig. 3 of [24] are very close, and seem to be at odds with Fig. 4 of [24].

The trend exhibited in the right-hand plots of Fig. 2 can be explained in relation to the response time of the system to water production and condensation. The slower the sweep rate the longer the time available to produce water in the catalyst layer, which leads to increasing saturation levels at 0.1 V (Fig. 4 shows the profiles of saturation and membrane water content during the sweep cycle at 10 mV s^{-1}). The higher saturation levels dictate

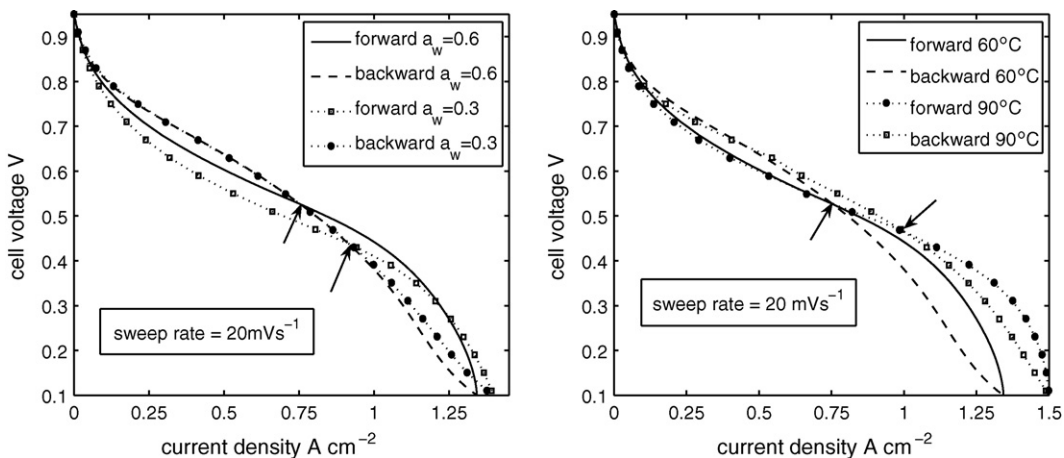


Fig. 5. The effects on the threshold value of variations in the water activity and temperature in the channels. The arrows indicate the locations of the thresholds.

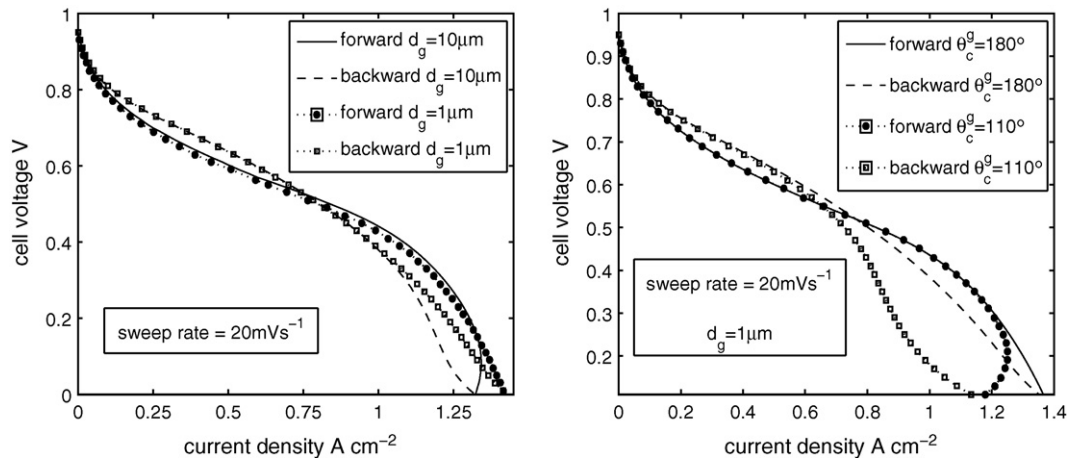


Fig. 6. The effects of variations in the pore size (d_g) and the contact angle (θ_c^g) in the GDL.

that the time required to evaporate the water is longer, therefore, in general, pushing the threshold current density to lower values and threshold cell voltage to higher values as the sweep rate is decreased. This, however, will be offset in some measure by the increased humidification of the membrane on the backward sweep when the saturations levels are greater, so that it is quite possible for the two processes to cancel each other.

3.2. Humidification and temperature effects

The effects of variations in the temperature and activity of the channel streams can be seen in Fig. 5. The left-hand figure demonstrates that the threshold phenomenon is much more pronounced for low water activity and in fact almost disappears as activity approaches unity (fully humidified). Although details of the experiments with humidified streams are not given in [24], the authors do state that in their experiments the threshold phenomenon was not apparent under these conditions. That this trend is observed is not surprising since the greater flooding of the CCL at higher activity demands that the time to evaporate enough liquid water on the backward sweep to transition from the mass-transport regime to the ohmic regime is longer, and in fact occurs towards the kinetic part of the curve. In this part of

the curve the current density is low and the cell voltage is high and their values are not dominated by the membrane resistance.

The right-hand plots in Fig. 5 show the effect of channel temperature: raising the temperature in the channels reduces the threshold voltage and increases the threshold current density. This result is in complete agreement with the potentiostatic sweep curves in [24]. The higher temperature in the channels causes reduced saturation levels because of a slower condensation rate. This results in a greater limiting current density at the higher temperature, despite the slight reduction in the reactant concentrations in the channels (by the ideal gas law). Consequently, a smaller volume of water is required to be evaporated on the backward sweep to reach the ohmic regime.

3.3. Effects of pore size, contact angle and micro-porous layer

We now turn our attention to the effects of two microstructural properties in the catalyst and gas-diffusion layers. Fig. 6 demonstrates the change in performance as the average pore size and contact angle in the GDL are varied.

As the pore size is decreased the saturation level decreases, a consequence of the greater capillary pressure gradients (the pore

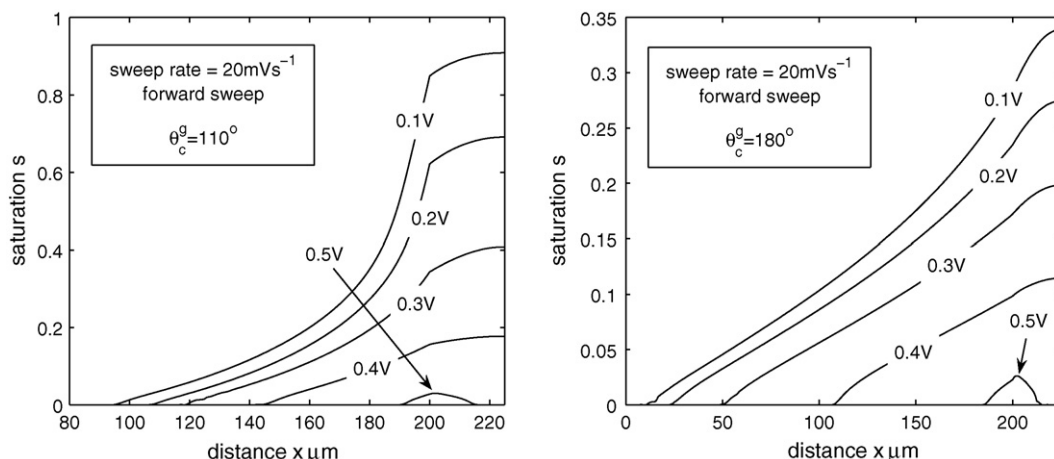


Fig. 7. A comparison of the profiles of saturation in the cathode during the forward sweeps of the two cases in Fig. 6 with $\theta_c^g = 180^\circ$ and $\theta_c^g = 110^\circ$.

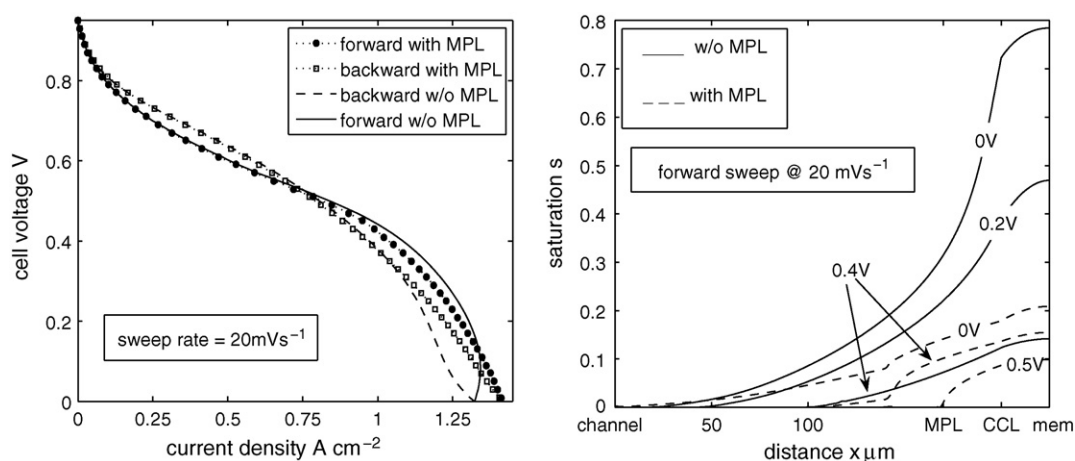


Fig. 8. The effects of a MPL, the right-hand figure showing saturation profiles with and without an MPL using the values in Tables 4 and 5.

size determines, at fixed porosity, the permeability according to the Kozeny–Carman law (5)). Thus the current density at 0.1 V is greater. The threshold point for $d_g = 1 \mu\text{m}$ occurs at a higher current density because of the decreased saturation, though the difference is small because of the competing process of membrane humidification.

A decreasing contact angle in the GDL leads to an increasing saturation because of its decreasing hydrophobicity (see Fig. 7). The right-hand plots in Fig. 6 show that in such cases the higher saturation forces the threshold point to lower current density and higher cell voltage. A competing effect, compounding the effect of increased membrane humidification, will be the greater retention of water on the backward sweep at $\theta_c^g = 110^\circ$.

Finally, we review one result relating to the effect of a MPL, shown in Fig. 8. The latter compares the sweep cycles with and without an MPL, where the total thickness of the gas diffusion medium (including the MPL) is kept constant at $200 \mu\text{m}$ and the MPL length is $30 \mu\text{m}$. The MPL can have a dramatic effect on the saturation levels in the cell. In general, the higher capillary pressure gradients in the smaller pores of the MPL lead to lower saturation levels, as seen in the right-hand plots of Fig. 8. The lower saturation levels force the current density at 0 V to a higher value. The current density at the threshold point is only slightly greater with the MPL than without, despite the very different levels of saturation on the two sweeps.

As with Fig. 6 it appears that with severe flooding in one case the increase in membrane hydration (and therefore conductivity) on the backward sweep can offset the flooding effect on the relative locations of the thresholds. Moreover, significant deviations in the threshold values are more easily seen when the forward and backward sweeps differ visibly in the ohmic part of the curve, as in Figs. 2 and 5.

4. Conclusions and future direction

We have demonstrated that a one-dimensional, transient model that fully accounts for liquid water and membrane hydration can qualitatively capture complex phenomena observed in fuel cell experiments. In particular, the hysteresis that is

often observed in laboratory experiments has been reproduced and explained. Multi-dimensional extensions of the model can answer questions related to the dimensions and geometry of the channels, anisotropic media and the strengths of the channel flows. On the other hand, the qualitative picture can at least be captured with the present model, which can therefore form the basis of an initial tool to screen MEA designs, combined with sweep cycling experiments. The latter are a convenient measure of performance, taking far less time than a steady-state polarization curve and possessing all of the features of the latter, including the competition between flooding and membrane hydration.

Furthermore, the transient aspect of the model provides scope for the study of other transient phenomena such as fast-transient polarization curves, startup and shutdown (with additional kinetic modelling) and freeze-start (with additional modelling of the thawing process). These are directions that are currently being pursued.

Acknowledgement

The authors are grateful to Ballard Power Systems for funding contributing to the present and ongoing research.

References

- [1] J. Cao, N. Djilali, Proceedings of the 10th Canadian Hydrogen Conference, 2000, pp. 447–456.
- [2] W. He, J. Yi, T.V. Nguyen, *AIChE Journal* 46 (2000) 2053–2064.
- [3] G. Lin, W. He, T. Van Nguyen, *J. Electrochem. Soc.* 151 (2004) A1999–A2006.
- [4] S. Mazumder, J.V. Cole, *J. Electrochem. Soc.* 150 (2004) A1510–A1517.
- [5] D. Natarajan, T.V. Nguyen, *J. Electrochem. Soc.* 148 (2001) A1324–A1335.
- [6] N.P. Siegel, M.W. Ellis, D.J. Nelson, M.R. von Spakovsky, *J. Power Sources* 115 (2003) 81–89.
- [7] N.P. Siegel, M.W. Ellis, D.J. Nelson, M.R. von Spakovsky, *J. Power Sources* 128 (2004) 173–184.
- [8] L.B. Wang, N.I. Wakayama, T. Okada, *Chem. Eng. Sci.* 60 (2005) 4453–4467.
- [9] Z.H. Wang, C.-Y. Wang, K.S. Chen, *J. Power Sources* 94 (2001) 40–50.

- [10] H. Ju, H. Meng, C.-Y. Wang, *Int. J. Heat Mass Transfer* 148 (2005) 1303–1315.
- [11] H. Meng, C.-Y. Wang, *J. Electrochem. Soc.* 152 (2005) A1733–A1741.
- [12] Y. Wang, C.-Y. Wang, *J. Electrochem. Soc.* 153 (2006) A1193–A1200.
- [13] U. Pasaogullari, C.-Y. Wang, *J. Electrochem. Soc.* 152 (2005) A380–A390.
- [14] L. You, H. Liu, *J. Power Sources* 155 (2006) 219–230.
- [15] C.-Y. Wang, P. Cheng, *J. Power Sources* 30 (1997) 93–196.
- [16] S. Um, C.-Y. Wang, K.S. Chen, *J. Electrochem. Soc.* 147 (2000) A4485–A4493.
- [17] S. Um, C.-Y. Wang, *J. Power Sources* 156 (2006) 211–223.
- [18] A. Vath, Z. Lemes, H. Mäncher, M. Sohn, N. Nicoloso, T. Hartkopf, *J. Power Sources* 157 (2006) 816–827.
- [19] S. Shimpalee, W.K. Lee, J.W. Van-Zee, H. Naseri-Neshat, *J. Power Sources* 156 (2006) 355–368.
- [20] Y. Wang, C.-Y. Wang, *Electrochim. Acta* 50 (2005) 1307–1315.
- [21] Y. Wang, C.-Y. Wang, *Electrochim. Acta* 51 (2006) 3924–3933.
- [22] C. Ziegler, H.M. Yu, J.O. Schumacher, *J. Electrochem. Soc.* 152 (2005) A1555–A1567.
- [23] C.-Y. Wang, *Chem. Rev.* 104 (2004) 4727–4766.
- [24] H.M. Yu, C. Ziegler, *J. Electrochem. Soc.* 153 (2006) A570–A575.
- [25] A.A. Shah, G.S. Kim, W. Gervais, A. Young, K. Promislow, J. Li, S. Yi, *J. Power Sources* 160 (2006) 1251–1268.
- [26] S. Wang, Y. Utaka, Y. Tadaki, *Heat Transf. Asian Res.* 35 (2006) 137–151.
- [27] X.L. Wang, H.M. Wang, J.L. Zhang, H.F. Xu, Z.Q. Tian, J. Chen, H.X. Zhong, Y.M. Liang, B.L. Yi, *Electrochim. Acta* 51 (2006) 4909–4915.
- [28] E. Middelmann, *Fuel Cells Bull.* (2002) 9–12.
- [29] M. Uchida, Y. Aoyama, N. Eda, O. Akira, *J. Electrochem. Soc.* 142 (1995) A4143–A4149.
- [30] S. Lister, G. McLean, *J. Power Sources* 130 (2004) 61–76.
- [31] H. Mizuhata, *J. Power Sources* 138 (2004) 25–30.
- [32] M.F. Serincan, S. Yesilyurt, in: Bradley, Drysdale, Makhviladze (Eds.), *Proceedings International Hydrogen Energy Congress and Exhibition IHEC 2005, Istanbul, Turkey, July 13–15, 2005*.
- [33] D.B. Genevey, Master's Thesis, Virginia Polytechnic Institute, 2004.
- [34] R.J. Fawcett, S. Hibberd, R.N. Singh, *Int. J. Mine Water* 3 (1984) 33–54.
- [35] B. Bird, W. Stewart, E. Lightfoot, *Transport Phenomena*, John Wiley and Sons, 2002.
- [36] Z. Ogumi, Z. Takehara, S. Yoshizawa, *J. Electrochem. Soc.* 131 (1984) A769–A772.
- [37] T.E. Springer, T.A. Zawodinski, S. Gottesfeld, *J. Electrochem. Soc.* 138 (1991) A2334–A2341.
- [38] W. Sun, B.A. Peppley, K. Karan, *Electrochim. Acta* 50 (2005) 3359–3374.
- [39] S. Motupally, A.J. Becker, J.W. Weidner, *J. Electrochem. Soc.* 147 (2000) A3171–A3177.
- [40] J.-H. Nam, M. Kaviani, *Int. J. Heat Mass Trans.* 46 (2003) 4595–4611.
- [41] J.T. Hinatsu, M. Mizuhata, H. Takenaka, *J. Electrochem. Soc.* 141 (1994) A1493–A1497.
- [42] S. Ge, X. Li, B. Yi, I.M. Hsing, *J. Electrochem. Soc.* 152 (2005) A1149–A1157.
- [43] A.Z. Weber, J. Newman, *J. Electrochem. Soc.* 152 (2005) A677–A688.
- [44] H. Weng, C.-Y. Wang, *J. Electrochem. Soc.* 151 (2004) A358–A367.
- [45] F.Y. Zhang, C.Y. Wang, *J. Electrochem. Soc.* 2 (2006) A225–A232.
- [46] X.G. Yang, F.Y. Zhang, A.L. Lubawy, C.-Y. Wang, *Electrochem. Solid-State Lett.* 7 (2004) A408–A411.
- [47] M.V. Williams, H.R. Kunz, J.M. Fenton, *J. Electrochem. Soc.* 151 (2004) A1617–A1627.
- [48] F. Jaouen, G. Lindbergh, G. Sundholm, *J. Electrochem. Soc.* 149 (2002) A437–A447.
- [49] T. Van Nguyen, W. He, in: W. Vielstich, A. Lamm, H. Gasteiger (Eds.), *Handbook of Fuel Cells - Fundamentals, Technology and Applications*, vol. 3 chapter 46, John Wiley & Sons, 2003.
- [50] U. Pasaogullari, C.-Y. Wang, K.S. Chen, *J. Electrochem. Soc.* 152 (2005) A1574–A1582.
- [51] C. Ziegler, A. Schmitz, M. Tranitz, E. Fontes, J.O. Schumacher, *J. Electrochem. Soc.* 151 (2004) A2028–A2041.
- [52] M.J. Lampinen, M. Fomino, *J. Electrochem. Soc.* 140 (1993) A3537–A3546.
- [53] R.H. Perry, D.W. Green, J.O. Maloney, *Perry's Chemical Engineers Handbook*, McGraw-Hill, 1984.
- [54] S.W. Cha, PhD Thesis, Stanford University, 2003.